





An Improved Ocean Surface Albedo Computational Scheme: Structure and Performance

Jian Wei¹ , Tong Ren² , Ping Yang², Steven F. DiMarco¹ , and Eli Mlawer³ 

¹Department of Oceanography, Texas A&M University, College Station, TX, USA, ²Department of Atmospheric Sciences, Texas A&M University, College Station, TX, USA, ³Atmospheric and Environmental Research, Lexington, MA, USA

Key Points:

- An improved ocean surface albedo (OSA) computational scheme is developed and implemented into an extensively used radiative transfer model
- The OSA scheme developed in this study considers multiple factors, and the computed OSA is reasonable compared to in-situ measurements
- The new OSA simulations are consistent with the Clouds and the Earth's Radiant Energy System OSA distribution on a global scale

Correspondence to:

J. Wei,
anser@tamu.edu

Citation:

Wei, J., Ren, T., Yang, P., DiMarco, S. F., & Mlawer, E. (2021). An improved ocean surface albedo computational scheme: Structure and performance. *Journal of Geophysical Research: Oceans*, 126, e2020JC016958. <https://doi.org/10.1029/2020JC016958>

Received 5 NOV 2020

Accepted 2 AUG 2021

Abstract Ocean surface albedo (OSA) is an important factor for the transfer of radiation in the coupled atmosphere-ocean system. By resolving the spectral variations of the reflective properties for incident direct and diffuse solar radiation, we develop an OSA computational scheme to study the impact of ocean biogeochemistry on the air-sea boundary condition of solar radiative transfer in the atmosphere. The new scheme is implemented for the General Circulation Model applications of the shortwave rapid radiative transfer model RRTMG_SW, a radiative transfer model used extensively in regional and global models. We show that a number of OSA schemes lead to underestimated results in comparison with in-situ measurements obtained at a site 25 km east of Virginia Beach. The scheme developed in this study considers multiple influential factors and is robust in terms of the mean absolute percentage error (MAPE) and the root mean square error in comparison with in-situ measurements. Furthermore, the new simulations are highly consistent with the Clouds and the Earth's Radiant Energy System (CERES) OSA distribution on a global scale. However, the theoretical results show slight differences compared with the CERES OSA under all sky conditions and overestimate the OSA in the subpolar Southern Ocean under clear sky conditions. The assumption of a uniform phase function, which neglects the spatial variability of the optical properties of oceanic particles, is largely responsible for the primary source of uncertainties in an OSA scheme.

Plain Language Summary Understanding the solar energy exchange between the atmosphere and the ocean is of primary importance in enhancing our ability to determine the radiative energy budget of the Earth. To describe the energy transport precisely, it is necessary to further study ocean surface albedo (OSA), the ratio of the upward radiation to the downward counterpart just above the air-sea interface. Oversimplified OSA algorithms in climate models lead to greatly varying estimates of how changes in reflected sunlight affect the global energy balance. This study develops an improved OSA computational scheme with an appropriate treatment of the ocean surface chlorophyll concentration-based inherent optical properties (IOPs) of the water column, which is implemented for the General Circulation Model applications of the shortwave rapid radiative transfer model RRTMG_SW. The new OSA scheme shows robust performance compared to the in-situ measurements from the Clouds and the Earth's Radiant Energy System (CERES) Ocean Validation Experiment on a regional scale, and the CERES surface fluxes products on a global scale. This scheme is expected to reduce uncertainties in the modeling of the energy budget of the coupled atmosphere-ocean system.

1. Introduction

Solar radiation is the fundamental energy source driving the Earth's climate system. Over the ocean, part of the incident solar energy penetrates the air-sea interface, which increases ocean heat content and influences many oceanographic processes, including ocean biogeochemistry, mixed layer stability, and oceanic circulation (Gupta et al., 1999). The remaining incident energy is reflected by the sea surface or is scattered by the hydrosols and water beneath the surface and then propagates upward. The ratio of the upward radiation to the incoming radiation at sea level, defined as ocean surface albedo (OSA), is a key factor determining the distribution of the solar radiation between the atmosphere and the ocean system (Enomoto, 2007). Errors in OSA may lead to biases in climate studies using a coupled atmosphere-ocean general circulation model (GCM) (Hall, 2004). Thus, an accurate estimation of OSA can benefit the modeling of the energy exchange between the atmosphere and the ocean system.

In the past several decades, various parameterizations of OSA have been developed for climate models based on both experimental observations and theoretical analyses. Briegleb et al. (1986) parameterized OSA as a function of solar zenith angle (SZA) based on observational data reported by Payne (1972), and this parameterization was adopted in the Community Climate System Model Coupler (CCSMC) (Kauffman et al., 2004). Schlick (1992) suggested a simplified OSA formula that includes the SZA in conjunction with an additional constant correction term. This simplified OSA formula was applied in the Minimal Advanced Treatments of Surface Interaction and Runoff (MARDIRO) (Takata et al., 2003). Based on aircraft measurements, Taylor et al. (1996) developed a similar OSA expression, and this parameterization has been used in the European Center for Medium-Range Forecasts (ECMWF) Integrated Forecast System (IFS) (ECMWF, 2019). However, the OSA is a function only of SZA in the aforementioned parameterizations.

Following Cox and Munk (1954) (CM54), Hansen et al. (1983) took sea surface roughness into account by suggesting OSA as a function of SZA and wind speed, which was used in the Goddard Institute for Space Studies General Circulation Model II (GISS GCM Model II). Using the ray-tracing technique, Preisendorfer and Mobley (1986) partitioned the incident radiation into direct and diffuse components, and calculated OSA based on SZA, wind speed, and fraction of the direct (or diffuse) radiation. This ray-tracing-based computational scheme was adopted in the Canadian Center for Climate Modeling and Analysis Atmospheric General Circulation Model version 4 (CCCMA-AGCM4) (Li et al., 2006). Based on a variety of simulated atmospheric and oceanic conditions from a coupled atmosphere-ocean radiative transfer model (COART) (Jin et al., 2006), Jin et al. (2011) developed a novel OSA parameterization that appropriately considers SZA, wind speed, and atmospheric and oceanic optical properties. In this novel OSA parameterization, the radiation is partitioned into direct and diffuse portions, and then the contributions of the surface and water to each portion are separately formulated. This parameterization has been used in the Action de Recherche Petite Echelle Grande Echelle V6.1 (ARPEGE-Climat V6.1) and Laboratoire de Météorologie Dynamique V5A (LMDZ V5A) (Séférian et al., 2018).

Due to the different OSA formulations, inconsistent OSA simulations have been reported in different global climate models (Li et al., 2006). A comparison of monthly mean albedo distributions from 20 global climate models and satellite observations (from Earth Radiation Budget Experiment [ERBE]) showed near-zero means of all of the modeled correlations with observations during November 1984 to February 1990 in large parts of global oceans (Bender et al., 2006). Through a thorough survey of the ocean optics parameterizations, we develop an OSA computational scheme for the widely used GCM application of the shortwave rapid radiative transfer model RRTMG_SW (Clough et al., 2005; Iacono et al., 2008; Mlawer & Clough, 1998) in this study. The remaining sections are organized as follows. Section 2 presents the formulation of the OSA scheme. Section 3 describes the sensitivity of the OSA scheme to its input parameters. The performance of the OSA scheme is evaluated in Section 4, and a summary is provided in Section 5.

2. The Formulation of the OSA Scheme

Surface albedo, or the reflectivity of a surface, is the ratio of the reflected radiative flux by the surface to the incident radiative flux. The ocean system reflects the incoming solar radiation (direct and diffuse) in three ways. The first is the reflection of incoming radiation by the foam-free fraction of the sea surface (i.e., sun glint). The second is the reflection of incoming radiation by whitecaps (or sea foam) at the sea surface. The third is the refraction of the upward radiation from the ocean interior by the sea surface. The contribution to the surface upwelling solar radiation through refraction is often called the water-leaving radiation. The formulations of the three pathways are presented in this section.

2.1. Sun Glint Reflection Formulation

For an ideal flat sea surface, the air-sea interface is usually regarded as a smooth surface, and sun glint reflectance can be obtained using the Fresnel formulas (Liou, 2002). However, because wind stress leads to temporally evolving sea states, the sea surface is almost always uneven. As a consequence, the air-sea interface is often treated as a collection of wave facets (Ramon et al., 2019). The CM54 (Cox & Munk, 1954) use a right-handed orthogonal coordinate system (P , X , Y and Z), where P represents the observed (origin) point on the wave surface, Z is the local vertical axis, PY points to the direction of the sun along the sea surface,

and PX is 90° clockwise from PY (or normal to the sun plane). We use the formula in CM54 to calculate the probability distribution function of wave slopes for a given wind speed U and wind direction χ_w . Based on the spherical trigonometry, the surface slope can be divided into two components, Z_x and Z_y , specified with respect to two orthogonal directions:

$$Z_x = \frac{-\sin(\theta_v)\sin(\phi_r)}{\cos(\theta_s) + \cos(\theta_v)}, \quad (1)$$

$$Z_y = \frac{\sin(\theta_s) + \sin(\theta_v)\cos(\phi_r)}{\cos(\theta_s) + \cos(\theta_v)}, \quad (2)$$

where θ_s is the SZA, θ_v is the viewing zenith angle (VZA), and ϕ_r is the relative azimuth angle, that is, the horizontal angle between the two planes specifying the SZA and VZA.

For a windblown surface, the distribution of the surface facet slopes is anisotropic with respect to the wind direction. To simplify the computational process, the coordinate system (P, X, Y , and Z) is rotated clockwise around the Z axis to obtain a new coordinate system (P', X', Y', Z') with PY' parallel to the wind direction, χ_w . The slope components of a specific surface facet in the new coordinate system are

$$Z'_x = \cos(\chi_w)Z_x + \sin(\chi_w)Z_y, \quad (3)$$

$$Z'_y = -\sin(\chi_w)Z_x + \cos(\chi_w)Z_y. \quad (4)$$

The probability distribution of surface facet slopes is quantified in CM54 in the following form:

$$P(Z'_x, Z'_y) = (2\pi\sigma'_x\sigma'_y)^{-1} \exp\left(-\frac{\xi^2 + \kappa^2}{2}\right) \cdot \left[1 - \frac{1}{2}C_{21}(\xi^2 - 1) - \frac{1}{6}C_{03}(\kappa^3 - 3\kappa) + \frac{1}{24}C_{40}(\xi^4 - 6\xi^2 + 3)\right] \cdot \left[1 + \frac{1}{4}C_{22}(\xi^2 - 1)(\kappa^2 - 1) + \frac{1}{24}C_{04}(\kappa^4 - 6\kappa^2 + 3)\right], \quad (5)$$

where $\xi = Z'_x / \sigma'_x$ and $\kappa = Z'_y / \sigma'_y$; σ'_x and σ'_y are the root mean squares of Z'_x and Z'_y , respectively; $\sigma'_x = 0.003 + 0.00192U$ and $\sigma'_y = 0.00316U$. Other coefficients are defined as follows (Cox & Munk, 1954):

$$C_{21} = 0.01 - 0.0086U, \quad (6)$$

$$C_{03} = 0.04 - 0.033U, \quad (7)$$

$$C_{40} = 0.40, \quad (8)$$

$$C_{22} = 0.12, \quad (9)$$

$$C_{04} = 0.23. \quad (10)$$

In addition, the shadowing effect needs to be considered when some surface facets obstruct other facets from a certain solar or viewing direction. Following Sancer (1969) and Gordon and Wang (1992), the shadowing function is given by

$$S(\theta_s, \phi_s, \theta_v, \phi_v) = \left[(1 - \Lambda(\varsigma_s))(1 - \Lambda(\varsigma_v)) \right]^{-1}, \quad (11)$$

where

$$\Lambda(\varsigma_s) = \frac{1}{2} \left[\frac{1}{\sqrt{\pi}} \frac{1}{\varsigma_s} \exp(-\varsigma_s^2) - \operatorname{erfc}(\varsigma_s) \right]. \quad (12)$$

In the above equation, ς_s is defined as

$$\zeta_s = \frac{|\cos \theta_s|}{\left(\sigma \sqrt{1 - \cos^2 \theta_s}\right)}, \quad (13)$$

where σ is the square root of the sum of the σ'_x and σ'_y squares in Equation 5; $\text{erfc}(\zeta)$ is the complementary error function (Abramowitz et al., 1988). $\Lambda(\zeta_v)$ is calculated in a similar way.

The sun glint reflectance, R_{sg} (dimensionless), is then calculated by

$$R_{sg}(\lambda, \theta_s, \phi_s, \theta_v, \phi_v, U, \chi_w) = \frac{\pi \rho_{as} \cdot P(Z'_x, Z'_y) \cdot S(\theta_s, \phi_s, \theta_v, \phi_v)}{4 \cos \theta_s \cos \theta_v \cos \theta_n}, \quad (14)$$

where ρ_{as} is the air-sea Fresnel reflection coefficient, as discussed in Liou (2002). θ_n is the tilt, that is, the zenith angle of the normal vector of the sea surface (Mobley, 1994), satisfying

$$\cos \theta_n = \frac{\cos \theta_s + \cos \theta_v}{\sqrt{2 + 2 \cos \psi}}, \quad (15)$$

where ψ is the scattering angle between the incident beam and a surface facet (Zhai et al., 2009), given by

$$\psi = \cos^{-1}(\cos \theta_s \cos \theta_v + \sin \theta_s \sin \theta_v \cos \phi_r). \quad (16)$$

2.2. Whitecaps Reflectance Formulation

When waves cannot sustain their crest on a sea surface, they break and entrain air into the seawater, and this air breaks up into bubbles, which rise to the sea surface (Monahan & O'Muircheartaigh, 1986) and form whitecaps. Accurate whitecaps spectral estimation is important in satellite-based inferences of aerosol optical thickness and ocean color (Chowdhary et al., 2005; Moore et al., 2000; Sayer et al., 2010). The structure of whitecaps is complex and may be described using several physical parameters, such as the geometrical thickness of the foam layer, the sizes and shapes of bubbles, the void fraction, and the types and stages of whitecaps (Kokhanovsky, 2004; Ma et al., 2015). Due to difficulties in modeling the realistic structure of whitecaps, whitecaps are usually simplified as a Lambertian reflector (Feng et al., 2016). Based on whitecap reflectance measurements in an indoor tank, Whitlock et al. (1982) parameterize the average whitecap reflectance using the water absorption coefficient. Koepke (1984) suggests that the whitecap reflectance is approximately constant in the visible spectral region but decrease with increasing wavelength in the near-infrared where water molecule absorption becomes important. Koepke (1984) also points out that the whitecap reflectance approaches zero and hence can be neglected when the wavelength exceeds 2.5 μm . Based on in-situ measurements, Frouin et al. (1996) suggest mean whitecap reflectances of around 0.4 in the visible region and 40%, 50%, and 85% smaller at wavelengths of 0.85, 1.02, and 1.65 μm , respectively. Field campaigns over both coastal and pelagic zones also show a reduction of reflectance with increasing wavelength in the near-infrared region (Moore et al., 1998; Nicolas et al., 2001). Kokhanovsky (2004) introduces an analytical model for calculating the whitecap reflectance, which is closely related to the water absorption at the sea surface. Using combined Lorenz-Mie and Monte Carlo scattering calculations, Ma et al. (2015) suggest that not only the water absorption but also the foam layer bubble size and thickness are important contributors to the whitecap reflectance. A recent study suggests a new water-absorption-coefficient-based whitecap reflectance parameterization from ultraviolet to shortwave infrared (Dierssen, 2019), which agrees in magnitude with previous whitecap reflectance measurements over different water types (Frouin et al., 1996). We therefore adopt this new parameterization in this study:

$$R_{wc}(\lambda) = 0.47x(\lambda)^3 - 1.62x(\lambda)^2 + 8.66x(\lambda) + 31.81, \quad (17)$$

where $R_{wc}(\lambda)$ (dimensionless) is the whitecap reflectance at the wavelength λ ; $x(\lambda) = \log(a_w(\lambda))$ and $a_w(\lambda)$ is the absorption coefficient of pure water (Dierssen, 2019).

The whitecap coverage, W , is the fraction of the sea surface covered by whitecaps. The whitecap fraction is often formulated by fitting spaceborne sea surface observations with respect to the surface wind speed,

commonly 10 m above the sea surface. The minimal wind speed for generating whitecaps is around 3 m/s (Monahan & O'Muircheartaigh, 1986). We adopt the formula of W given by Albert et al. (2016) in this study:

$$W = 10.77 + 10^{-5} (U + 1.789)^2, \quad (18)$$

where U is the 10 m wind speed. This parameterization of whitecap coverage applies to $U = 3\text{--}20$ m/s, generally covering the wind speed range over oceans in the earth system models (S  f  rian et al., 2018).

2.3. Water-Leaving Reflectance Formulation

The ocean color remote sensing reflectance above the sea surface, or water-leaving reflectance, R_{wl} (unit: sr^{-1}) is defined as the ratio of the upwelling radiance that is, backscattered out of the ocean to the downwelling irradiance just above the sea surface. R_{wl} is highly dependent on the inherent optical properties (IOPs) in the seawater and the viewing geometry (i.e., incident angle, viewing angle, and relative azimuth) (Mobley, 1994). In this study, we focus on optically deep waters, where the reflection from the ocean floor can be ignored.

2.3.1. Bio-Optical Model

The total absorption coefficient, $a(\lambda)$, has four components:

$$a(\lambda) = a_w(\lambda) + a_{ph}(\lambda) + a_d(\lambda) + a_g(\lambda), \quad (19)$$

where $a_w(\lambda)$ is the water absorption for wavelength λ ranging from 200 to 5,000 nm. In this study, estimates of $a_w(\lambda)$ are taken from the measurements by Segelstein (1981) in 200–300 nm, Morel et al. (2007) in 300–350 nm, Lee et al. (2015) in 350–550 nm, and Pope and Fry. (1997) in 550–700 nm spectral ranges. In the infrared range ($\lambda > 700$ nm), an average of measurements of $a_w(\lambda)$ in Segelstein (1981), Wieliczka et al. (1989), and Max and Chapados (2009) is used. $a_{ph}(\lambda)$ is the phytoplankton absorption; $a_d(\lambda)$ is the absorption by non-algal particles; and $a_g(\lambda)$ is the absorption by the Chromophoric Dissolved Organic Matter (CDOM).

About 44% of the incident solar radiation within the wavelength range 400–700 nm at the sea surface is photosynthetically active (Churilova et al., 2020). Following previous studies (Brewin et al., 2011; Devred et al., 2011; Roy et al., 2013; Varunan & Shanmugam, 2015), we estimate the total $a_{ph}(\lambda)$ between 400 and 700 nm using a linear combination of the absorption contributions by different phytoplankton size groups, including the pico- (size: $<2 \mu\text{m}$), nano- ($2\text{--}20 \mu\text{m}$), and micro-phytoplankton ($>20 \mu\text{m}$) groups:

$$a_{ph}(\lambda) = P^*(\lambda)C_P + N^*(\lambda)C_N + M^*(\lambda)C_M, \quad (20)$$

where $P^*(\lambda)$, $N^*(\lambda)$, and $M^*(\lambda)$ are the size-specific absorption coefficients of pico-, nano-, and micro-phytoplankton, respectively; and C_P , C_N , and C_M are the corresponding chlorophyll concentrations, expressed as a function of the total chlorophyll concentration (chl) (Brewin et al., 2017).

The radiation in the ultraviolet region ($\lambda < 400$ nm) only accounts for about 4% of the total incoming radiation at the sea surface (Lee et al., 2005). Phytoplankton absorption between 300 and 400 nm is small compared to the visible spectral region. Because the $P^*(\lambda)$, $N^*(\lambda)$, and $M^*(\lambda)$ coefficients in Equation 20 are currently not available in the ultraviolet (Varunan & Shanmugam, 2015), the size-classed calculation cannot be performed in this wavelength region. We therefore approximate the phytoplankton absorption between 300 and 400 nm by the following exponential form:

$$a_{ph}(\lambda) = A(\lambda) \cdot \text{chl}^{1-B(\lambda)}, \quad (21)$$

where $A(\lambda)$ and $B(\lambda)$ are from in-situ measurements and radiative transfer simulations available in Vasilkov et al. (2005). Less than 5% of total incoming radiation at the surface in the ultraviolet region falls in wavelengths shorter than 300 nm due to strong gas absorption in the atmosphere (Kerr & Fioletov, 2008). Within the $\lambda < 300$ nm range, the total absorption $a(\lambda)$ comes primarily from CDOM and non-algal particles, with absorption coefficients $a_g(\lambda)$ and $a_d(\lambda)$ several orders of magnitude larger than $a_{ph}(\lambda)$ (Hannach & Sigleo, 1998; Yamashita & Tanoue, 2009). We therefore neglect phytoplankton absorption when $\lambda < 300$ nm. Beyond 700 nm, phytoplankton absorption is also negligible (Mobley, 1994) and water absorption is the

primary contributor to the total absorption (Ohlmann et al., 2000). Hence, we also neglect phytoplankton absorption when $\lambda > 700$ nm in this study.

In addition to phytoplankton, non-algal particles and CDOM also contribute to the total absorption. The sources and sinks of CDOM have been well documented (D'Sa & DiMarco, 2009). We adopt exponentially decaying expressions introduced by previous studies (Roesler & Perry, 1995; Twardowski et al., 2004) to calculate the absorption contributions by non-algal particles and CDOM:

$$a_d(\lambda) = a_d(440) \cdot \exp[-S_d \cdot (\lambda - 440)], \quad (22)$$

$$a_g(\lambda) = a_g(440) \cdot \exp[-S_g \cdot (\lambda - 440)], \quad (23)$$

where $a_d(440)$ and $a_g(440)$ are the reference absorption coefficients at 440 nm, which are empirically linked to the total chlorophyll concentration (chl) (Bricaud et al., 2010; Morel & Maritorena, 2001). In this study, S_d and S_g are obtained from Roesler and Perry (1995) and Twardowski et al. (2004), respectively.

The total backscattering coefficient, b_b , can be divided into two components:

$$b_b(\lambda) = b_{bp}(\lambda) + b_{bw}(\lambda), \quad (24)$$

where $b_{bp}(\lambda)$ is the particle (phytoplankton and non-algal particles) backscattering coefficient and $b_{bw}(\lambda)$ is the water backscattering coefficient. We take the water scattering coefficient $b_w(\lambda)$ from Zhang and Hu (2009) and Zhang et al. (2009) and estimate the water backscattering coefficient using the Rayleigh scattering relationship $b_{bw}(\lambda) = 0.5b_w(\lambda)$. Following Brewin et al. (2012), $b_{bp}(\lambda)$ is evaluated by considering contributions by different phytoplankton size groups separately:

$$\begin{aligned} b_{bp}(\lambda) = & b_{bp,1,2}^*(\lambda_0) (\lambda / \lambda_0)^{-\gamma_{1,2}} C_{1,2}^m \left[1 - \exp(-S_{1,2} [chl]) \right] \\ & + b_{bp,3}^*(\lambda_0) (\lambda / \lambda_0)^{-\gamma_3} \left\{ [chl] - C_{1,2}^m \left[1 - \exp(-S_{1,2} [chl]) \right] \right\}, \\ & + b_{bp}^k(\lambda_0) (\lambda / \lambda_0)^{-\gamma_k} \end{aligned} \quad (25)$$

where $b_{bp,i}^*(\lambda)$ is the chlorophyll-specific particulate backscattering coefficient for each of the phytoplankton size groups at wavelength λ with $i = 1, 2$, and 3 representing pico-, nano-, and micro-phytoplankton, respectively. $b_{bp}^k(\lambda)$ is a constant background particle backscattering component mainly contributed by non-algal particles. The reference wavelength λ_0 is 470 nm and the eight parameters in Equation 25 ($C_{1,2}^m$, $S_{1,2}$, $b_{bp,1,2}^*(\lambda_0)$, $b_{bp,3}^*(\lambda_0)$, $b_{bp}^k(\lambda_0)$, $\gamma_{1,2}$, γ_3 , and γ_k) are taken from Brewin et al. (2012). In addition, inelastic scattering effects, such as Raman scattering and fluorescence (Zhai et al., 2015, 2017, 2018), are small in broadband radiative transfer calculations and hence are not included in this study.

2.3.2. Water-Leaving Reflectance

In the past decades, a number of models were developed for simplified calculations of ocean reflectance for remote sensing applications, because the underlying physical processes are otherwise complicated. Including the total absorption $a(\lambda)$ and backscattering $b_b(\lambda)$ in these simplified models allows the models to be applicable to ocean color remote sensing implementations. Gordon et al. (1988) developed a nadir-viewed polynomial model for subsurface remote sensing reflectance r_{rs} , which is defined in terms of the ratio of subsurface upwelling radiance to subsurface downwelling irradiance. Based on the work by Gordon et al. (1988) and Albert and Mobley (2003) suggested a fourth-order polynomial for modeling r_{rs} with different viewing angles and wind speeds. Lee et al. (1994, 2004) separated molecular and particulate scattering events and modeled r_{rs} using a second-order polynomial. Park and Ruddick. (2005) suggested a fourth-order polynomial fitting of r_{rs} based on the ratio of seawater scattering to the total scattering. In He et al. (2017), the contributions of molecular and particulate scattering to r_{rs} were also considered based on their backward volume scattering function shapes. Using the radiative transfer equation in Zaneveld. (1995) and Twardowski and Tonizzo (2018) formulated r_{rs} as a function of several variables, including the average

cosine of the downwelling light field $\overline{\mu_d}$, and the ratio of the diffuse upwelling attenuation coefficient K_{Lu} to the asymptotic attenuation coefficient K_∞ .

If an r_{rs} model is selected for an OSA scheme, a divergence factor \mathfrak{R} is needed to convert r_{rs} to the water-leaving reflectance (above-surface remote sensing reflectance) R_{wl} . The factor \mathfrak{R} describes the radiance that enters into the air from the water below the interface (Gordon, 2005; Morel & Gentili, 1993, 1996; Morel et al., 2002), satisfying

$$R_{wl}(\lambda, \Omega, U, \text{IOPs}) = \mathfrak{R} \cdot r_{rs}(\lambda, \Omega', \text{IOPs}), \quad (26)$$

where Ω and Ω' are the sun-view angular geometry above and underneath the sea surface, respectively. The r_{rs} to R_{wl} conversion can be avoided, if an R_{wl} model is used instead (Gordon et al., 1988). Lee et al. (2011) developed an R_{wl} model with two terms accounting for molecule and particle scatterings, separately. Hlaing et al. (2012) suggested a third-order polynomial fitting of R_{wl} with model coefficients determined by the single backscattering albedo $b_b(\lambda)/(a(\lambda) + b_b(\lambda))$.

In the new OSA scheme, the R_{wl} model in Lee et al. (2011) is adopted for simplicity:

$$R_{wl}(\lambda, \Omega, \text{IOPs}) = \left(G_0^w(\Omega) + G_1^w(\Omega) \cdot \frac{b_{bw}(\lambda)}{a(\lambda) + b_b(\lambda)} \right) \cdot \frac{b_{bw}(\lambda)}{a(\lambda) + b_b(\lambda)} + \left(G_0^p(\Omega) + G_1^p(\Omega) \cdot \frac{b_{bp}(\lambda)}{a(\lambda) + b_b(\lambda)} \right) \cdot \frac{b_{bp}(\lambda)}{a(\lambda) + b_b(\lambda)}, \quad (27)$$

where $G_0^w(\Omega)$, $G_1^w(\Omega)$, $G_0^p(\Omega)$, and $G_1^p(\Omega)$ are coefficients that are dependent on the angular geometry and the particle phase function. These coefficients were fitted using HydroLight simulations with two pre-selected particle phase functions representing the particle scattering of an assemblage of particles, that is, non-algal particles (mineral like particles) and phytoplankton. Petzold average phase function was used for non-algal particles, and Fournier and Forand phase function with a backscattering-to-scattering ratio as 1% was used for phytoplankton. More details can be found in Lee et al. (2011). Henceforth we use the term “the blended Petzold average and 1% Fournier and Forand phase function” to describe the ocean particle phase function of the R_{wl} model in this study. HydroLight is a commercial radiative transfer model that computes the optics of natural water bodies, with all orders of multiple scattering considered (Mobley, 1994).

2.4. Computation of the OSA

After the sun glint, whitecaps, and water-leaving reflectances are determined, the combination of the three leads to the sea surface bidirectional reflectance factor R_{BRF} , which is defined as the ratio of the reflected radiant flux from the surface to the reflected radiant flux from a perfectly diffuse surface under the same condition of illumination and observation (Feng et al., 2016; Schaepman-Strub et al., 2006):

$$R_{BRF}(\lambda, \theta_s) = \text{WR}_{wc}(\lambda) + (1 - W) \left(R_{sg}(\lambda, \theta_s) + \pi R_{wl}(\lambda, \theta_s) \right), \quad (28)$$

where W is the whitecap fraction defined in Section 2.2. The incident sunlight at the sea surface consists of the direct and ambient diffuse components, which are treated separately by introducing the directional-hemispherical reflectance (R_{DHR} , is also reported as black-sky albedo) and the bi-hemispherical reflectance (R_{BHR} , is also referred to as white-sky albedo) (Lucht et al., 2000; Schaepman-Strub et al., 2006). R_{DHR} describes the diffuse reflection of the direct incident beam by the sea surface over the whole hemisphere (illumination comes from a sole direction), and is a function of the SZA (Lucht et al., 2000; Schaepman-Strub et al., 2006). For a given SZA, integration of R_{BRF} over all viewing zenith and relative azimuth angles yields R_{DHR} :

$$R_{DHR}(\lambda, \theta_s) = \frac{1}{\pi} \int_0^{2\pi} \int_0^{\pi/2} R_{BRF}(\lambda, \theta_s) \cos \theta_v \sin \theta_v d\theta_v d\phi_r, \quad (29)$$

where θ_v is the viewing zenith angle and ϕ_r is the relative azimuth angle. R_{BHR} describes the reflection of diffuse downwelling incident beam (illumination arises from the whole of the sky), which is considered

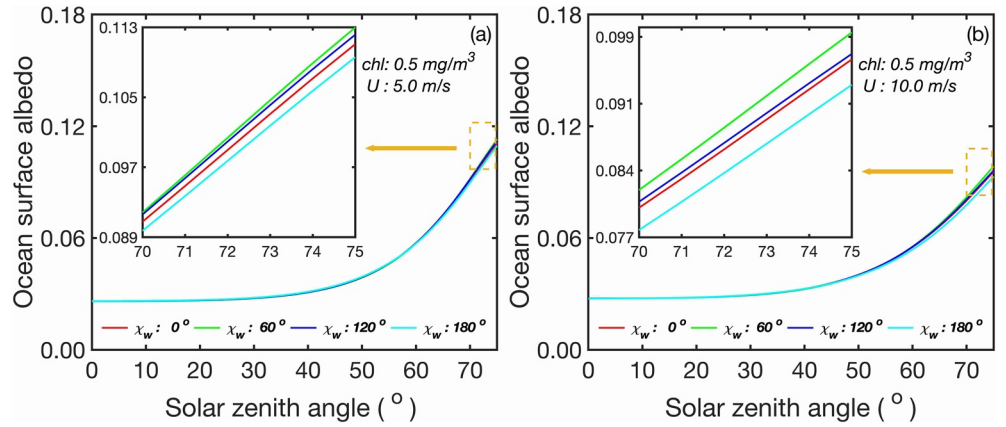


Figure 1. Comparison of a broadband (200–4,000 nm) application of our ocean surface albedo scheme as functions of solar zenith angles under different wind directions in a clear sky condition. (a) Wind speed 5.0 m/s. (b) Wind speed 10.0 m/s. Chlorophyll concentration (chl) is set to 0.5 mg/m³.

approximately isotropic (Lucht et al., 2000; Schaepman-Strub et al., 2006). R_{BHR} is obtained by integrating R_{DHR} over all incident zenith angles:

$$R_{BHR}(\lambda) = 2 \int_0^{\pi/2} R_{DHR}(\lambda, \theta_s) \cos \theta_s \sin \theta_s d\theta_s, \quad (30)$$

where θ_s is the incident zenith angle.

Due to the computational complexity of the spherical albedo introduced by integrations over the solar and viewing geometry in Equations 29 and 30, simplified approximations of the spherical albedo are often used in practice. Following Rutan et al. (2009), we evaluate the plane albedo R_{DHR} at a “diffuse” SZA ($\theta_{s_diffuse}$) for the spherical albedo R_{BHR} computation:

$$R_{BHR}(\lambda) = R_{DHR}(\lambda, \theta_{s_diffuse}), \quad (31)$$

where $\theta_{s_diffuse}$ is the “diffuse” SZA and is set to the Gaussian quadrature point in the two-stream approximations ($\theta_{s_diffuse} = 53^\circ$) (Liou, 2002; Rutan et al., 2009).

Using Equation 31 to calculate the ocean surface spherical albedo in our OSA scheme, $OSA(\lambda)$ is obtained by combining R_{DHR} and R_{BHR} (Feng et al., 2016; Sayer et al., 2010):

$$OSA(\lambda) = (1 - F_{dif}) R_{DHR}(\lambda) + F_{dif} R_{BHR}(\lambda), \quad (32)$$

where F_{dif} is a weighting factor representing the fraction of the diffuse radiation to the total incident radiation at the surface. The $OSA(\lambda)$ defined as such ignores the higher order terms of the downwelling diffuse radiation. A broadband OSA, OSA_{bb} , between λ_{min} and λ_{max} can be derived by integrating $OSA(\lambda)$ from λ_{min} to λ_{max} (Séférian et al., 2018):

$$OSA_{bb} = \frac{\int_{\lambda_{min}}^{\lambda_{max}} OSA(\lambda) E(\lambda) d\lambda}{\int_{\lambda_{min}}^{\lambda_{max}} E(\lambda) d\lambda}, \quad (33)$$

where $E(\lambda)$ is the standard solar spectrum NRLSSI2 (Coddington et al., 2016). We incorporate our OSA scheme into RRTMG_SW by calculating OSA_{bb} for each of the 14 RRTMG_SW bands using Equation 33 (see Appendix).

3. Sensitivity Analysis of the OSA Scheme

As previously mentioned, in this study the OSA is parameterized as a function of five variables, SZA, chlorophyll concentration (chl), wind speed U , wind direction χ_w , and surface diffuse radiation fraction. Figure 1 shows broadband (200–4,000 nm) OSA variations with SZA, U , and χ_w under a clear sky condition.

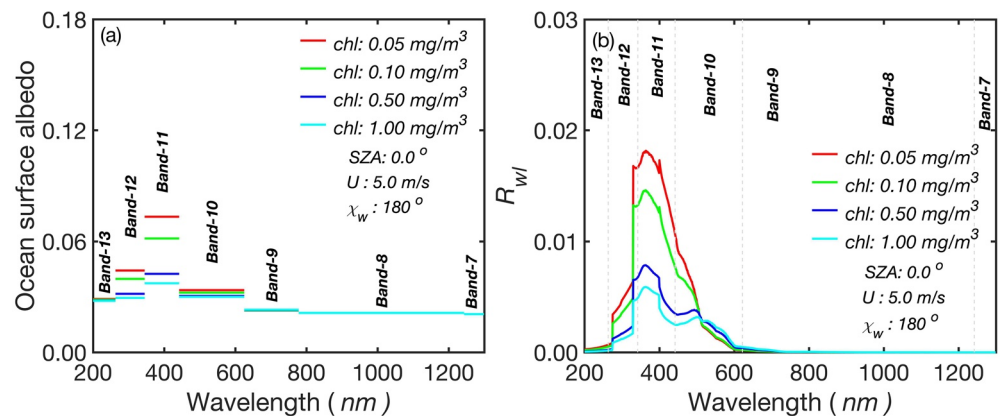


Figure 2. (a) ocean surface albedo in the RRTMG_SW Bands 7–13 (for band details, see Table A1) and (b) Spectral variation of the above-surface remote sensing reflectance R_{wl} . Cases are shown with different chlorophyll concentrations (chl) in a clear sky condition with SZA = 0°, wind speed of 5 m/s, and wind direction of 180°.

As shown in Figure 1, OSA increases with increasing SZA. The difference in OSA caused by different wind speeds is small when SZA is lower than 60°. When SZA exceeds 60°, OSA decreases with increasing wind speed. For instance, when the wind speed increases from 5.0 to 10.0 m/s, OSA decreases by about 3.9% at SZA = 60° and about 14.0% at SZA = 75°. Because the shadowing effect of surface waves increases with increasing SZA and wind speed (Feng et al., 2016), the influence of the wind direction on OSA is noticeable only when SZA > 50° and the wind speed is high (Figure 1).

Figure 2 shows spectral variations of clear sky OSA and R_{wl} with the chlorophyll concentration within the wavelength range 200–1,300 nm that includes the RRTMG_SW Bands 7–13. Within the wavelength range, OSA is higher and more sensitive to (chl) at wavelengths between 300 and 700 nm (Bands 10–12) than at other wavelengths (Figure 2a). The increased sensitivity of OSA to (chl) between 300 and 700 nm agrees with the increased sensitivity of R_{wl} to (chl) within the wavelength interval (Figure 2b). Between 300 and 700 nm, the absorption by molecules (a_w) is relatively low (Lee et al., 2015; Varunan & Shanmugam, 2015; Vasilkov et al., 2005), and hence the R_{wl} and OSA variations are driven mostly by the chlorophyll concentration variation. As shown in Figure 2, OSA and R_{wl} decrease with increasing (chl) between 300 and 470 nm (Bands 11 and 12) due to increased phytoplankton absorption (a_{ph}) with increasing (chl). However, the dependence of OSA and R_{wl} upon (chl) changes sign between 470 and 700 nm (Bands 9 and 10) (Figure 2), presumably due to the fact that enhanced backscattering exceeds enhanced absorption within this wavelength range as (chl) rises (Jin et al., 2004). For wavelengths <300 nm, CDOM and detritus (non-algal particles) absorption is the main cause of sunlight attenuation in seawater (Hannach & Sigleo, 1998; Yamashita & Tanoue, 2009). As a consequence, OSA and R_{wl} are less sensitive to (chl) at wavelengths <300 nm (Band 13) (Figure 2). Although ultraviolet radiation at wavelengths shorter than 285 nm (i.e., UV-C) rarely reaches the earth surface due to the strong oxygen and ozone absorption in the stratosphere (Kerr & Fioletov, 2008; Mlawer & Clough, 1998), we retain the OSA calculation at those wavelengths so that the OSA scheme is applicable to all the RRTMG_SW Bands. At wavelengths >700 nm, the total absorption (a) is predominantly accounted for by molecular absorption (a_w) (Ohlmann et al., 2000; Segelstein, 1981) and hence OSA and R_{wl} are almost independent from the (chl) variability (Figure 2).

4. Evaluation of the OSA Scheme Performance

To assess the robustness of the new OSA computational (O-OSA) scheme, we validate our scheme against in-situ broadband (200–4,000 nm) sea surface radiative flux measurements from the Clouds and the Earth's Radiant Energy System (CERES) (Wielicki et al., 1996) Ocean Validation Experiment (COVE). The COVE radiative flux measurements were made at a marine observational station in the coastal Atlantic Ocean approximately 25 km off the Virginia coastline (Rutledge & Smith, 2003). In addition, we also compare the COVE measurements with other OSA schemes reported in previous studies, as documented in Table 1. As in Chai and Draxler (2014), the root mean square error (RMSE) and mean absolute percentage error

Table 1
The Ocean Surface Albedo (OSA) Computational Schemes Adopted in the Comparison

OSA schemes	Input variables	Applications	References
B-OSA	SZA	CCSMC	Briegleb et al. (1986); Kauffman et al. (2004)
S-OSA	SZA	MARDIRO	Schlick (1992); Takata et al. (2003)
T-OSA	SZA	ECMWF-IFS	ECMWF (2019); Taylor et al. (1996)
H-OSA	SZA, Wind speed	GISS GCM Model II	Hansen et al. (1983)
J-OSA	Viewing geometry, wind speed, IOPs, and diffuse fraction	ARPEGE-Climat V6.1; LMDZ V5A	Jin et al. (2011); Séférian et al. (2018)
O-OSA	Viewing geometry, wind speed, wind direction, IOPs, and diffuse fraction	RRTMG_SW	N/A

Note. The letter before OSA is the initial of the first author defining the scheme except O-OSA.
SZA, solar zenith angle.

(MAPE) are used to quantify the difference between each of the selected OSA schemes and the COVE measurements. Moreover, by making use of the global monthly CERES Edition 4.1 surface downward shortwave direct and diffusive radiation fluxes (Kato et al., 2018), we compare O-OSA scheme with the one used in deriving the CERES surface fluxes (Jin et al., 2004; Rutan et al., 2015) on a global scale.

4.1. In-Situ Measurements

The COVE sea surface upward and downward shortwave radiation measurements were accessed from the Data Publisher for Earth & Environmental Science Tool (PANGAEA), which archives the COVE data from the Baseline Surface Radiation Network (BSRN) for public use (Driemel et al., 2018). The upward radiation measurements are only available from December 2013 to December 2014 and hence the measurements during this period are used for OSA scheme validations. Sea surface wind data were obtained from a buoy at the COVE station from the National Buoy Data Center (NBDC). Because no chlorophyll concentration (chl) data was available from COVE, chlorophyll concentrations were taken from satellite daily operational products from the Ocean Biology Processing Group at NASA's Goddard Space Flight Center (NASA Goddard Space Flight Center, 2014). A 5×5 box of satellite pixels centered at the COVE site was searched to obtain the average of all available (chl) retrievals within the box (Bailey & Werdell, 2006). The size of each satellite pixel is 1 km^2 . In total, there are 66 matched samples with SZA from 18.4° to 61.5° , wind speed U from 0.3 to 14.0 m/s, wind direction χ_w from 4.0° to 338.0° , and (chl) from 1.25 to 3.71 mg/m^3 . The COVE OSA is computed as the ratio of measured broadband upwelling to downwelling radiation.

Figure 3 compares the selected OSA estimates with the corresponding COVE OSA measurements. As expected, all parameterized OSAs increase with SZA in general, with the schemes that depend on SZA only (B-OSA, S-OSA, and J-OSA) increasing monotonically with SZA. Other selected schemes (H-OSA, J-OSA, and O-OSA) show small OSA fluctuations as SZA increases due to influences by factors other than SZA. In agreement with previous studies (e.g., Jin et al., 2002), overall, all selected schemes underestimate the COVE OSA measurement. Table 2 documents the RMSE and MAPE for each of the selected OSA schemes, as compared with the COVE measurement. Among the OSA schemes, the two schemes (J-OSA and O-OSA) that take multiple influential factors into account show the best agreement with the COVE measurement, as suggested by their smallest RMSE and MAPE. Differences between J-OSA and O-OSA include the following: (a) J-OSA considers the optical properties of the whole phytoplankton population from Morel and Maritorena (2001), whereas O-OSA separates the absorption contributions by different phytoplankton size groups based on more recent studies (Brewin et al., 2012; Varunan & Shanmugam, 2015). (b) J-OSA's whitecap reflectance from Koepke (1984) assumes a constant reflectance $R_{wc}(\lambda) = 0.55$, whereas O-OSA uses the latest whitecap reflectance parameterization (Dierssen, 2019) that is, a function of spectral water absorption $a_w(\lambda)$. Moreover, J-OSA adopts the whitecap coverage of Monahan and O'Muircheartaigh (1980), while O-OSA takes the parameterization by Albert et al. (2016). (c) The sun glint reflectance R_{sg} in J-OSA is dependent only on the wind speed, whereas R_{sg} in O-OSA depends on both the wind speed and direction. (d) J-OSA is built from the coupled ocean-atmosphere radiative transfer (COART) model (Jin et al., 2006, 2011)

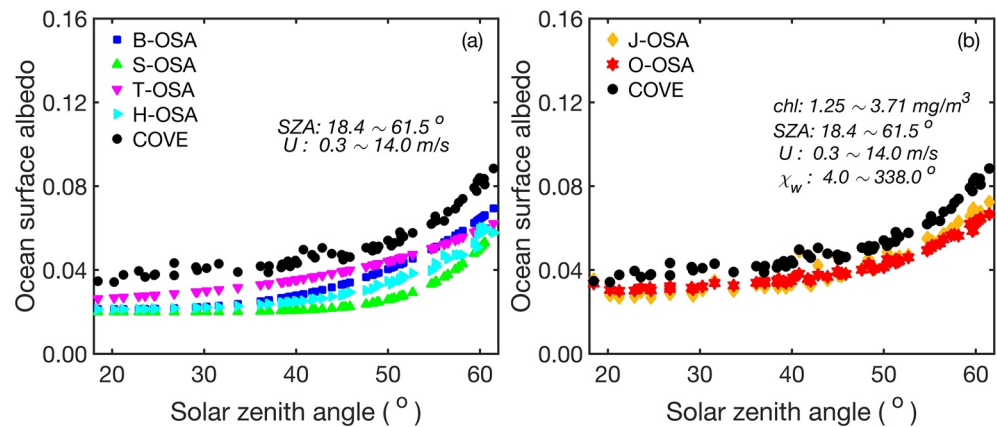


Figure 3. Comparison of the ocean surface albedo (OSAs) derived from different computational schemes and the COVE measurements (66 matches). (a) B-OSA, S-OSA, and T-OSA schemes only depend on solar zenith angle and H-OSA also depends on U . (b) J-OSA and the scheme in this study (O-OSA) take both atmospheric and oceanic conditions into account.

in which a Petzold's particle scattering phase function is assumed, whereas O-OSA uses a synthetic particle phase function, specifically, the blended Petzold average and 1% Fournier and Forand phase function (Lee et al., 2011).

Compared to the COVE measurement, uncertainty sources of O-OSA include the following: (a) The mean (chl) retrieval over an area of 25 km^2 is used to approximate the (chl) situation at the COVE site. The spatial resolution mismatch may cause uncertainties in the (chl) input to O-OSA. (b) O-OSA uses the blended Petzold average and 1% Fournier and Forand phase function (Lee et al., 2011). The representativeness of the mean phase function may cause uncertainties in the water-leaving reflectance R_{wl} estimation in O-OSA. (c) While not included in our calculations, inorganic suspended sediment scattering is also important in the OSA determination, particularly in the coastal area because the COVE site is only 25 km offshore with a water depth of 11 m. (d) In addition, seabed reflection also contributes to the R_{wl} , but O-OSA assumes optically deep waters and ignores shallow bottom reflection.

4.2. Satellite Observations

This subsection compares O-OSA with Jin et al. (2004) on a global scale, using the CERES Edition 4.1 monthly shortwave (300–5,000 nm) surface radiation flux product. Both the upward and downward direct and diffuse monthly surface shortwave radiative fluxes during March–May 2019 were used for the comparison. The wind data during this period were obtained from the ECMWF ERA-Interim monthly products (Dee et al., 2011). Chlorophyll concentrations were taken from the monthly operational products from the

Ocean Biology Processing Group at NASA's Goddard Space Flight Center (NASA Goddard Space Flight Center, 2014). We estimated the monthly mean SZAs using the standard method from Gupta et al. (2001). All data were averaged in each grid box with a spatial resolution of $1.0^\circ \times 1.0^\circ$.

The global and zonal mean distributions of all sky and clear sky OSA estimations from O-OSA and CERES are shown in Figures 4 and 5a, respectively. Because OSA generally increases with SZA (Figure 3), the global clear sky OSA distribution shows a strong meridional variation with large values in high latitude oceans and small values in tropical oceans (Figures 4a, 4b and 5a). The all sky OSA distribution shows a much weaker meridional variation (Figures 4c, 4d and 5a), because the incident solar radiation at the surface is dominated by the diffuse component due to the atmospheric scattering under all sky conditions (Figure 6b). As shown in Figures 4 and 5a, O-OSA highly agrees with Jin et al. (2004) in the CERES

Table 2
RMSE and MAPE (Percent) of Each of the Selected Ocean Surface Albedo (OSA) Schemes as Compared With the COVE Measurement

	RMSE	MAPE
B-OSA	0.0154	30.22
S-OSA	0.0257	48.19
T-OSA	0.0128	21.50
H-OSA	0.0204	38.54
J-OSA	0.0105	18.86
O-OSA	0.0119	19.83

MAPE, mean absolute percentage error; RMSE, root mean square error.

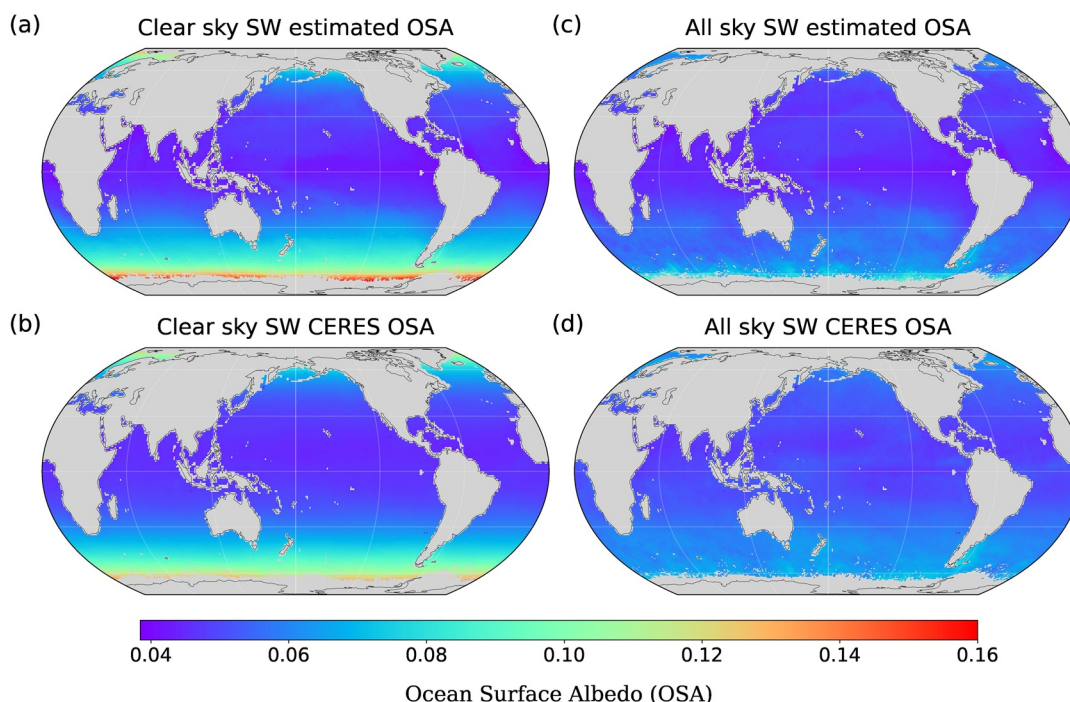


Figure 4. Global monthly mean ocean surface albedo (OSAs) during March–May 2019. (a) and (c) are clear sky and all sky OSA estimations based on O-OSA scheme, respectively. (b) and (d) are corresponding clear sky and all sky OSA based on Jin et al. (2004), which is used in the derivation of the CERES surface radiation fluxes. (Note Jin et al., 2004 derive the OSA with a look up table (LUT) made from a validated coupled ocean-atmosphere radiative transfer model (Jin et al., 2002, 2005). The OSA LUT is a function of SZA, wind speed, chlorophyll concentration, and transmissivity of atmospheric cloud/aerosol, which strongly affects the fraction of diffuse radiation at the sea level).

surface radiation flux product in terms of the geographical pattern, especially for the regions between 60°S and 70°N, with zonal mean differences ranging from −13% to 5% (Figure 5b).

Under clear sky conditions, however, O-OSA overestimates the CERES OSA in the subpolar Southern Ocean (>60°S) (Figures 4a, 4b, 5 and 7a). Preisendorfer and Mobley (1986) and Henderson et al. (2003) suggested that about 10%–15% of the rays at a viewing direction have been reflected more than one time due to wave shadowing but the influence of sunlight multiple reflectances is small when the wind speed U is lower than 10 m/s and the solar zenith angle SZA is smaller than 80°. O-OSA considers the shadowing effect (Equations 11–13) in the sun glint reflectance R_g calculation, but the correction of the shadowing effect we adopt only accounts for the first-order wave mutual shadowing or blocking (Ross & Dion, 2007). The neglecting of sunlight multiple reflections may explain the O-OSA overestimation in the subpolar Southern Ocean (with large wind stress (e.g., $U > 10$ m/s) and low solar elevations (e.g., SZA > 80°); figures are not

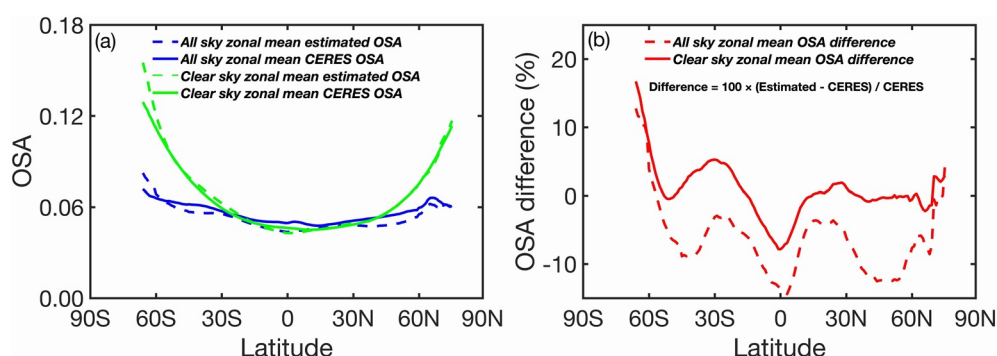


Figure 5. (a) Zonal mean of the global monthly mean ocean surface albedo (OSAs) under both clear sky and all sky conditions during March–May 2019 and (b) Zonal mean relative OSA differences.

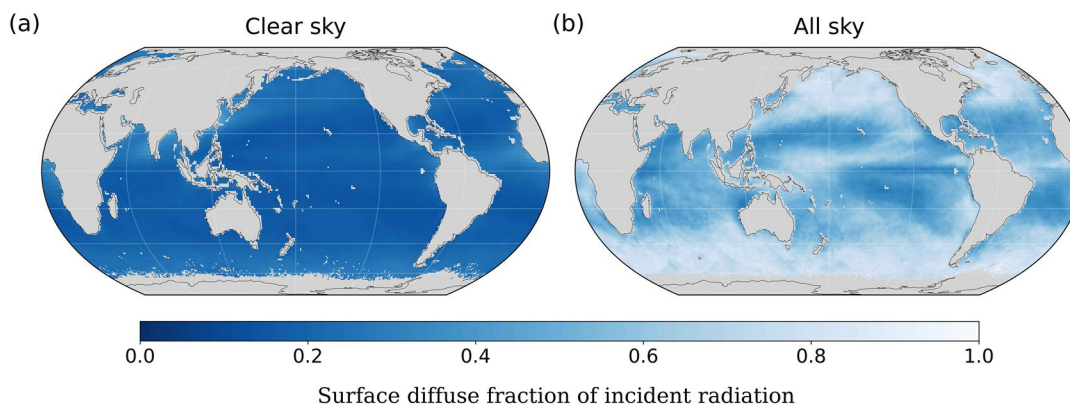


Figure 6. Monthly mean CERES surface diffuse radiation fraction during March–May 2019 under (a) Clear sky and (b) All sky conditions.

shown here). In addition, on a global scale, we assume a fixed ocean particle (phytoplankton and non-algal particles) phase function in the derivation of R_{DHR} and R_{BHR} . Hence, regional variability of ocean particle scattering properties causes uncertainties in the R_{DHR} and R_{BHR} , which translate into the OSA uncertainty. However, the influence of phase function on the OSA is smaller than that of SZA. Because the all sky OSA in O-OSA is largely determined by R_{BHR} with a fixed diffuse SZA (Equation 31), the small OSA differences between O-OSA and CERES under all sky conditions should result from the different phase function selections. Overall, O-OSA agrees well with the CERES OSA under both clear sky and all sky conditions in terms of their small RMSEs and MAPEs (Figure 7).

5. Summary

OSA plays an important role in the global surface radiation budget. We developed an OSA computational (O-OSA) scheme based on parameterizations of whitecaps and IOPs taken from recent studies. The new scheme is applicable to a spectral regime from 200 to 5,000 nm and has been incorporated into RRTMG_SW. Comparing the aforesaid O-OSA scheme and other schemes with in-situ surface broadband shortwave radiation flux measurements, the new scheme and that developed by Jin et al. (2011) consider multiple influential factors and lead results consistent with measurements. Based on a further comparison of the O-OSA with Jin et al. (2004) in the global CERES surface radiation flux, O-OSA highly agrees with the CERES global OSA distribution, although O-OSA shows small biases compared with the CERES OSA under all sky conditions and overestimates the CERES OSA in the subpolar Southern Ocean under clear sky conditions.

The blended Petzold average and 1% Fournier and Forand phase function is used in the O-OSA scheme. However, ocean particles have various sizes and shapes (e.g., Mukherjee et al., 2018), and hence a fixed particle phase function makes the spatial variability of particle scattering properties a primary uncertainty

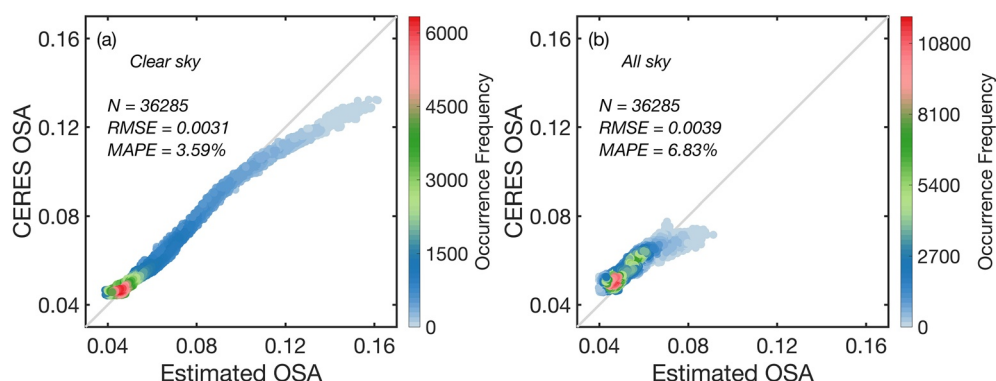


Figure 7. Scatterplots of the global monthly mean Clouds and the Earth's Radiant Energy System ocean surface albedo (OSAs) versus the OSA estimations by O-OSA during March–May 2019 under (a) Clear sky and (b) All sky conditions.

source of the OSA scheme. Moreover, due to limited OSA measurements, we only evaluated the O-OSA scheme against in-situ measurements in a broadband (200–4,000 nm) sense. In-situ OSA measurements in narrower bands, if available, will help evaluate the OSA scheme in specific wavelength intervals, such as the 14 RRTMG_SW bands designed for optimal estimation of atmospheric gas optical properties.

The O-OSA scheme is derived from the radiative transfer calculation of light propagation through the sea surface that additionally incorporates ocean biogeochemistry (i.e., an ocean surface chlorophyll concentration-based system). The adoption of O-OSA in global climate models would improve the representation of physics at the air-sea boundary. This scheme is a function of SZA (light source position), (chl) (operating light attenuation in ocean interior), U and χ_w (regulating a windblown sea surface and sea foam fraction). In current climate models, the nutrient-phytoplankton-zooplankton-detritus (NPZD) methods are extensively used in modeling ocean biogeochemistry, while the degree of complexity varies among different models (Fu et al., 2016; Laufkotter et al., 2015; Nakamura & Oka, 2019). The O-OSA scheme adopts (chl) for calculating solar radiation attenuation of the water column, adjusting the amount of penetrated light in the waterside. The change of sunlight penetration in the ocean may affect ocean heat content, physiological and biochemical features, stability of the ocean mixed layer, or even other phenomena ocean currents, and so forth (Gupta et al., 1999). In other words, the O-OSA scheme more accurately reproduces the energy exchange between the atmosphere and the ocean through ocean biogeochemistry in the climate models. All input parameters to O-OSA are prognostics in earth system models, we expect that it is straightforward to implement this scheme into models, particularly for those using RRTMG in their radiation calculations.

Appendix A: Incorporation of the New OSA Scheme Into the RRTMG_SW

In RRTMG_SW, surface albedo is calculated as the difference between unity and the surface emissivity, specified as a user input. Once surface emissivity is determined, the main module of source codes calls other modules and the radiative fluxes are computed, for example, upward flux, downward direct flux, downward diffuse flux, and so forth. Three options are provided by RRTMG_SW for the emissivity input (Figure A1) (Iacono et al., 2008): (Control variable IEMIS = 0) each band has a surface emissivity equal to 1.0; (IEMIS = 1) each band has the same surface emissivity specified by the user; (IEMIS = 2) each band has a different surface emissivity specified by the user. We added a fourth option (IEMIS = 3), which applies to the ocean surface only (Figure A1). By selecting IEMIS = 3, the new OSA scheme introduced in this study is called, and additional inputs (chlorophyll concentration, wind speed, and wind direction) are required. As RRTMG_SW specifies downward flux calculations at each atmospheric layer in the form of direct and diffuse components, R_{DHR} and R_{BHR} are appropriate for quantifying the reflection features of downward direct and diffuse fluxes at the sea level (Equations 29 and 31). Hence, the fraction F_{diff} is not required to be given. In addition, the surface emissivity for Band 14 (Table A1) still needs to be set by the user, because band 14 approaches the thermal infrared region and is beyond the scope of this study.

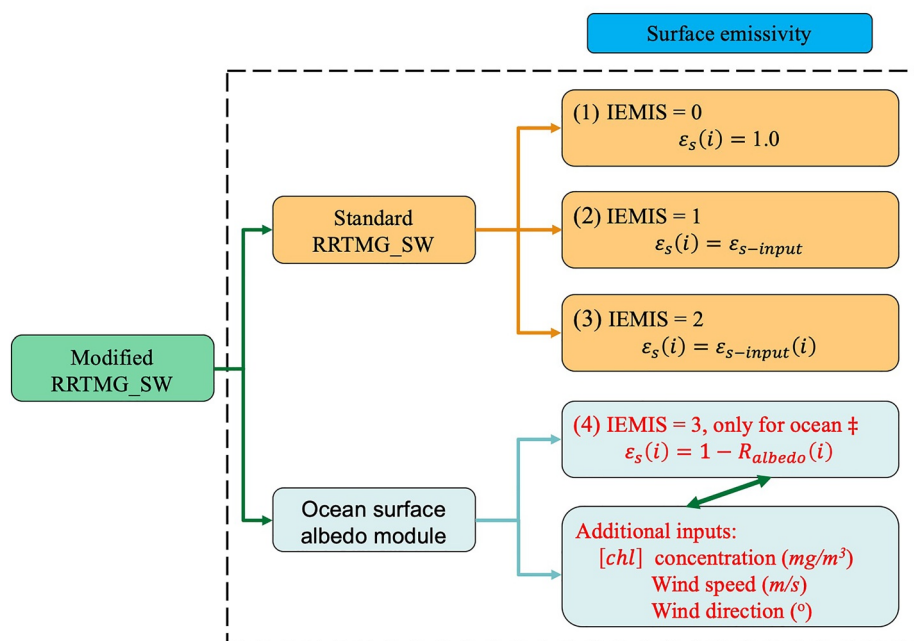


Figure A1. A schematic diagram of the RRTMG_SW with the new ocean surface albedo scheme included. ‡: $\epsilon_s(i)$ includes both direct and diffuse emissivities.

Table A1

RRTMG_SW Bands and Associated Major Absorbing Gases (Mlawer & Clough, 1998)

Band number	Wavenumber (cm ⁻¹)	Wavelength (nm)	Lower atmosphere	Middle/upper atmosphere
			(1,050–96 mb)	(96–0.01 mb)
1	2600–3250	3846.1–3076.9	H ₂ O, CH ₄	CH ₄
2	3250–4000	3076.9–2500.0	H ₂ O, CO ₂	H ₂ O, CO ₂
3	4000–4650	2500.0–2150.5	H ₂ O, CH ₄	CH ₄
4	4650–5150	2150.5–1941.8	H ₂ O, CO ₂	CO ₂
5	5150–6150	1941.8–1626.0	H ₂ O, CH ₄ ^a	H ₂ O, CH ₄ ^a
6	6150–7700	1626.0–1298.7	H ₂ O, CO ₂	H ₂ O, CO ₂
7	7700–8050	1298.7–1242.4	H ₂ O, O ₂	O ₂
8	8050–12,850	1242.4–778.2	H ₂ O	N/A
9	12,850–16,000	778.2–625.0	H ₂ O, O ₂ , O ₃ ^a	O ₂ , O ₃ ^a
10	16,000–22,650	625.0–441.5	H ₂ O, O ₃ ^a	O ₃ ^a
11	22,650–29,000	441.5–344.8	N/A	N/A
12	29,000–38,000	344.8–263.1	O ₃	O ₃
13	38,000–50,000	263.1–200.0	O ₃ , O ₂	O ₃ , O ₂
14	820–2600	12,195.1–3846.1	H ₂ O	CO ₂

^aMinor gases.

Data Availability Statements

The sea surface radiative flux measurements from the Clouds and the Earth's Radiant Energy System (CERES) Ocean Validation Experiment (COVE) are available from the Baseline Surface Radiation Network (BSRN) project via the Data Publisher for Earth & Environmental Science Tool (PANGAEA) (<https://bsrn.awi.de/data/data-retrieval-via-pangaea/>). Daily sea surface wind data are retrievable from the National Buoy Data Center (NBDC) for station CHLV2 (https://www.ndbc.noaa.gov/station_page.php?station=chlv2). Daily and Monthly chlorophyll concentrations are available from the Ocean Biology Processing Group at NASA's Goddard Space Flight Center (<https://oceancolor.gsfc.nasa.gov/>). Monthly CERES Edition 4.1 monthly shortwave surface radiation flux products are available from the CERES project (<https://ceres.larc.nasa.gov/data/>). The European Center for Medium-Range Forecasts (ECMWF) ERA-Interim monthly surface wind field can be accessed from the website (<https://www.ecmwf.int/>).

Acknowledgments

This study was supported by the National Science Foundation (AGS-1632209) and partly by the endowment funds related to the David Bullock Harris Chair in Geosciences at the TAMU College of Geosciences (02-512231-10000). We are grateful to Dr. S. Schroeder who helped edit the manuscript. We appreciate the editor and three anonymous reviewers for their constructive and helpful comments on this study. The computations involved in this study were performed using Texas A&M High Performance Research Computing Facilities.

References

- Abramowitz, M., Stegun, I. A., & Romer, R. H. (1988). *Handbook of mathematical functions with formulas, graphs, and mathematical tables (applied mathematics series 55)*. US Department of Commerce, National Bureau of Standards. Retrieved from http://people.math.sfu.ca/~cbm/aands/abramowitz_and_stegun.pdf
- Albert, A., & Mobley, C. (2003). An analytical model for subsurface irradiance and remote sensing reflectance in deep and shallow case-2 waters. *Optics Express*, 11(22), 2873. <https://doi.org/10.1364/oe.11.002873>
- Albert, M. F. M. A., Anguelova, M. D., Manders, A. M. M., Schaap, M., & De Leeuw, G. (2016). Parameterization of oceanic whitecap fraction based on satellite observations. *Atmospheric Chemistry and Physics*, 16(21), 13725–13751. <https://doi.org/10.5194/acp-16-13725-2016>
- Bailey, S. W., & Werdell, P. J. (2006). A multi-sensor approach for the on-orbit validation of ocean color satellite data products. *Remote Sensing of Environment*, 102(1–2), 12–23. <https://doi.org/10.1016/j.rse.2006.01.015>
- Bender, F. A. M., Rodhe, H., Charlson, R. J., Ekman, A. M. L., & Loeb, N. (2006). 22 views of the global albedo—Comparison between 20 GCMs and two satellites. *Tellus, Series A: Dynamic Meteorology and Oceanography*, 58(3), 320–330. <https://doi.org/10.1111/j.1600-0870.2006.00181.x>
- Brewin, R. J. W., Ciavatta, S., Sathyendranath, S., Jackson, T., Tilstone, G., Curran, K., et al. (2017). Uncertainty in ocean-color estimates of chlorophyll for phytoplankton groups. *Frontiers in Marine Science*, 4, 1–22. <https://doi.org/10.3389/fmars.2017.00104>
- Brewin, R. J. W., Dall'Olmo, G., Sathyendranath, S., & Hardman-Mountford, N. J. (2012). Particle backscattering as a function of chlorophyll and phytoplankton size structure in the open-ocean. *Optics Express*, 20(16), 17632–17652. <https://doi.org/10.1364/oe.20.017632>
- Brewin, R. J. W., Devred, E., Sathyendranath, S., Lavender, S. J., & Hardman-Mountford, N. J. (2011). Model of phytoplankton absorption based on three size classes. *Applied Optics*, 50(22), 4535–4549. <https://doi.org/10.1364/AO.50.004535>
- Bricaud, A., Babin, M., Claustre, H., Ras, J., & Tièche, F. (2010). Light absorption properties and absorption budget of Southeast Pacific waters. *Journal of Geophysical Research*, 115(8), 1–19. <https://doi.org/10.1029/2009JC005517>
- Briegleb, B. P., Minnis, P., Ramanathan, V., & Harrison, E. (1986). Comparison of regional clear-sky albedos inferred from satellite observations and model computations. *Journal of Climate and Applied Meteorology*, 25(2). [https://doi.org/10.1175/1520-0450\(1986\)025<0214:corcsa>2.0.co;2](https://doi.org/10.1175/1520-0450(1986)025<0214:corcsa>2.0.co;2)
- Chai, T., & Draxler, R. R. (2014). Root mean square error (RMSE) or mean absolute error (MAE)?—Arguments against avoiding RMSE in the literature. *Geoscientific Model Development*, 7(3), 1247–1250. <https://doi.org/10.5194/gmd-7-1247-2014>
- Chowdhary, J., Cairns, B., Mishchenko, M. I., Hobbs, P. V., Cota, G. F., Redemann, J., et al. (2005). Retrieval of aerosol scattering and absorption properties from photopolarimetric observations over the ocean during the CLAMS experiment. *Journal of the Atmospheric Sciences*, 62(4), 1093–1117. <https://doi.org/10.1175/jas3389.1>
- Churilova, T. Y., Suslin, V. V., Moiseeva, N. A., & Efimova, T. V. (2020). Phytoplankton bloom and photosynthetically active radiation in coastal waters. *Journal of Applied Spectroscopy*, 86(6), 1084–1091. <https://doi.org/10.1007/s10812-020-00944-0>
- Clough, S. A., Shephard, M. W., Mlawer, E. J., Delamere, J. S., Iacono, M. J., Cady-Pereira, K., et al. (2005). Atmospheric radiative transfer modeling: A summary of the AER codes. *Journal of Quantitative Spectroscopy and Radiative Transfer*, 91(2), 233–244. <https://doi.org/10.1016/j.jqsrt.2004.05.058>
- Coddington, O., Lean, J. L., Pilewskie, P., Snow, M., & Lindholm, D. (2016). A solar irradiance climate data record. *Bulletin of the American Meteorological Society*, 97(7), 1265–1282. <https://doi.org/10.1175/BAMS-D-14-00265.1>
- Cox, C., & Munk, W. (1954). Measurement of the roughness of the sea surface from photographs of the sun's glitter. *Journal of the Optical Society of America*, 44(11), 838–850. <https://doi.org/10.1364/josa.44.000838>
- Dee, D. P., Uppala, S. M., Simmons, A. J., Berrisford, P., Poli, P., Kobayashi, S., et al. (2011). The ERA-Interim reanalysis: Configuration and performance of the data assimilation system. *Quarterly Journal of the Royal Meteorological Society*, 137(656), 553–597. <https://doi.org/10.1002/qj.828>
- Devred, E., Sathyendranath, S., Stuart, V., & Platt, T. (2011). A three component classification of phytoplankton absorption spectra: Application to ocean-color data. *Remote Sensing of Environment*, 115(9), 2255–2266. <https://doi.org/10.1016/j.rse.2011.04.025>
- Dierssen, H. M. (2019). Hyperspectral measurements, parameterizations, and atmospheric correction of whitecaps and foam from visible to shortwave infrared for ocean color remote sensing. *Frontiers in Earth Science*, 7, 1–18. <https://doi.org/10.3389/feart.2019.00014>
- Driemel, A., Augustine, J., Behrens, K., Colle, S., Cox, C., Cuevas-Agulló, E., et al. (2018). Baseline surface radiation network (BSRN): Structure and data description (1992–2017). *Earth System Science Data*, 10(3), 1491–1501. <https://doi.org/10.5194/essd-10-1491-2018>
- D'sa, E. J., & DiMarco, S. F. (2009). Seasonal variability and controls on chromophoric dissolved organic matter in a large river-dominated coastal margin. *Limnology & Oceanography*, 54(6), 2233–2242. <https://doi.org/10.4319/lo.2009.54.6.2233>
- ECMWF. (2019). *IFS documentation CY46r1: Part IV: Physical processes*. Retrieved from <https://www.ecmwf.int/en/elibrary/19748-part-iv-physical-processes>
- Enomoto, T. (2007). Ocean surface albedo in AFES. *JAMSTEC Report of Research and Development*, 6(0), 21–30. <https://doi.org/10.5918/jamstecr.6.21>

- Feng, Y., Liu, Q., Qu, Y., & Liang, S. (2016). Estimation of the ocean water albedo from remote sensing and meteorological reanalysis data. *IEEE Transactions on Geoscience and Remote Sensing*, 54(2), 850–868. <https://doi.org/10.1109/TGRS.2015.2468054>
- Frouin, R., Schwindling, M., & Deschamps, P. Y. (1996). Spectral reflectance of sea foam in the visible and near-infrared: In situ measurements and remote sensing implications. *Journal of Geophysical Research*, 101(C6), 14361–14371. <https://doi.org/10.1029/96JC00629>
- Fu, W., Randerson, J. T., & Keith Moore, J. (2016). Climate change impacts on net primary production (NPP) and export production (EP) regulated by increasing stratification and phytoplankton community structure in the CMIP5 models. *Biogeosciences*, 13(18), 5151–5170. <https://doi.org/10.5194/bg-13-5151-2016>
- Gordon, H. R. (2005). Normalized water-leaving radiance: Revisiting the influence of surface roughness. *Applied Optics*, 44(2), 241–248. <https://doi.org/10.1364/AO.44.000241>
- Gordon, H. R., Brown, O. B., Evans, R. H., Brown, J. W., Smith, R. C., Baker, K. S., & Clark, D. K. (1988). A semianalytic radiance model of ocean color. *Journal of Geophysical Research*, 93(D9), 10909–10924. <https://doi.org/10.1029/JD093iD09p10909>
- Gordon, H. R., & Wang, M. (1992). Surface-roughness considerations for atmospheric correction of ocean color sensors II: Error in the retrieved water-leaving radiance. *Applied Optics*, 31(21), 4247–4260. <https://doi.org/10.1364/ao.31.004261>
- Gupta, S. K., Kratz, D., Stackhouse, P. W., & Wilber, A. C. (2001). *The langley parameterized shortwave algorithm (LPSA) for surface radiation budget Studies, NASA tech reports (Version 1.0)*. Retrieved from <http://ntrs.nasa.gov/archive/nasa/casi.ntrs.nasa.gov/20020022720.pdf>
- Gupta, S. K., Ritchey, N. A., Wilber, A. C., Whitlock, C. H., Gibson, G. G., & Stackhouse, P. W. (1999). A climatology of surface radiation budget derived from satellite data. *Journal of Climate*, 12(8), 2691–2710. [https://doi.org/10.1175/1520-0442\(1999\)012<2691:acosrb>2.0.co;2](https://doi.org/10.1175/1520-0442(1999)012<2691:acosrb>2.0.co;2)
- Hall, A. (2004). The role of surface albedo feedback in climate. *Journal of Climate*, 17(7), 1550–1568. [https://doi.org/10.1175/1520-0442\(2004\)017<1550:TROSAF>2.0.CO;2](https://doi.org/10.1175/1520-0442(2004)017<1550:TROSAF>2.0.CO;2)
- Hannach, G., & Sigleo, A. C. (1998). Photoinduction of UV-absorbing compounds in six species of marine phytoplankton. *Marine Ecology Progress Series*, 174, 207–222. <https://doi.org/10.3354/meps174207>
- Hansen, J., Russell, G., Rind, D., Stone, P., Lacis, A., Lebedeff, S., et al. (1983). Efficient three-dimensional global models for climate studies: Models I and II. *Monthly Weather Review*, 111(4), 609–662. [https://doi.org/10.1175/1520-0493\(1983\)111<0609:ETDGMF>2.0.CO;2](https://doi.org/10.1175/1520-0493(1983)111<0609:ETDGMF>2.0.CO;2)
- He, S., Zhang, X., Xiong, Y., & Gray, D. (2017). A bidirectional subsurface remote sensing reflectance model explicitly accounting for particle backscattering shapes. *Journal of Geophysical Research: Oceans*, 122(11), 8614–8626. <https://doi.org/10.1002/2017JC013313>
- Henderson, B. G., Theiler, J., & Villeneuve, P. (2003). The polarized emissivity of a wind-roughened sea surface: A Monte Carlo model. *Remote Sensing of Environment*, 88(4), 453–467. <https://doi.org/10.1016/j.rse.2003.09.003>
- Hlaing, S., Gilerson, A., Harmel, T., Tonizzo, A., Weidemann, A., Arnone, R., & Ahmed, S. (2012). Assessment of a bidirectional reflectance distribution correction of above-water and satellite water-leaving radiance in coastal waters. *Applied Optics*, 51(2), 220–237. <https://doi.org/10.1364/AO.51.000220>
- Iacono, M. J., Delamere, J. S., Mlawer, E. J., Shephard, M. W., Clough, S. A., & Collins, W. D. (2008). Radiative forcing by long-lived greenhouse gases: Calculations with the AER radiative transfer models. *Journal of Geophysical Research Atmospheres*, 113(13), 2–9. <https://doi.org/10.1029/2008JD009944>
- Jin, Z., Charlock, T., Rutledge, K., Fang, Y., & Yi, W. (2011). A parameterization of spectral and broadband ocean surface albedo. *Optics Express*, 19(27), 26429–26443. <https://doi.org/10.1364/OE.19.026429>
- Jin, Z., Charlock, T. P., & Rutledge, K. (2002). Analysis of broadband solar radiation and albedo over the ocean surface at COVE. *Journal of Atmospheric and Oceanic Technology*, 19(10), 1585–1601. [https://doi.org/10.1175/1520-0426\(2002\)019<1585:AOSRA>2.0.CO;2](https://doi.org/10.1175/1520-0426(2002)019<1585:AOSRA>2.0.CO;2)
- Jin, Z., Charlock, T. P., Rutledge, K., Cota, G., Kahn, R., Redemann, J., et al. (2005). Radiative transfer modeling for the CLAMS experiment. *Journal of the Atmospheric Sciences*, 62(4), 1053–1071. <https://doi.org/10.1175/JAS3351.1>
- Jin, Z., Charlock, T. P., Rutledge, K., Stamnes, K., & Wang, Y. (2006). Analytical solution of radiative transfer in the coupled atmosphere-ocean system with a rough surface. *Applied Optics*, 45(28), 7443–7455. <https://doi.org/10.1364/AO.45.007443>
- Jin, Z., Charlock, T. P., Smith, W. L., & Rutledge, K. (2004). A parameterization of ocean surface albedo. *Geophysical Research Letters*, 31(22), 1–4. <https://doi.org/10.1029/2004GL021180>
- Kato, S., Rose, F. G., Rutan, D. A., Thorsen, T. J., Loeb, N. G., Doelling, D. R., et al. (2018). Surface irradiances of edition 4.0 Clouds and the Earth's Radiant Energy System (CERES) Energy Balanced and Filled (EBAF) data product. *Journal of Climate*, 31(11), 4501–4527. <https://doi.org/10.1175/JCLI-D-17-0523.1>
- Kauffman, B. G., Jacob, R., Craig, T., & Larson, W. G. (2004). *The CCSM coupler version 6.0 documentation, the CCSM project*. Retrieved from <http://www.cesm.ucar.edu/models/ccsm3.0/cpl6/>
- Kerr, J. B., & Fioletov, V. E. (2008). Surface ultraviolet radiation. *Atmosphere—Ocean*, 46(1), 159–184. <https://doi.org/10.3137/ao.460108>
- Koepke, P. (1984). Effective reflectance of oceanic whitecaps. *Applied Optics*, 23(11), 1816–1824. <https://doi.org/10.1364/ao.23.001816>
- Kokhanovsky, A. A. (2004). Spectral reflectance of whitecaps. *Journal of Geophysical Research: Oceans*, 109(5), 1–9. <https://doi.org/10.1029/2003JC002177>
- Laufkötter, C., Vogt, M., Gruber, N., Aita-Noguchi, M., Aumont, O., Bopp, L., et al. (2015). Drivers and uncertainties of future global marine primary production in marine ecosystem models. *Biogeosciences*, 12(23), 6955–6984. <https://doi.org/10.5194/bg-12-6955-2015>
- Lee, Z., Carder, K. L., Hawes, S. K., Steward, R. G., Peacock, T. G., & Davis, C. O. (1994). Model for the interpretation of hyperspectral remote-sensing reflectance. *Applied Optics*, 33(24), 5721. <https://doi.org/10.1364/ao.33.005721>
- Lee, Z., Wei, J., Voss, K., Lewis, M., Bricaud, A., & Huot, Y. (2015). Hyperspectral absorption coefficient of “pure” seawater in the range of 350–550 nm inverted from remote sensing reflectance. *Applied Optics*, 54(3), 546–558. <https://doi.org/10.1364/ao.54.000546>
- Lee, Z. P., Carder, K. L., & Du, K. P. (2004). Effects of molecular and particle scatterings on the model parameter for remote-sensing reflectance. *Applied Optics*, 43(25), 4957–4964. <https://doi.org/10.1364/AO.43.004957>
- Lee, Z. P., Du, K., Voss, K. J., Zibordi, G., Lubac, B., Arnone, R., & Weidemann, A. (2011). An inherent-optical-property-centered approach to correct the angular effects in water-leaving radiance. *Applied Optics*, 50(19), 3155–3167. <https://doi.org/10.1364/AO.50.003155>
- Lee, Z. P., Du, K. P., Arnone, R., Liew, S. C., & Penta, B. (2005). Penetration of solar radiation in the upper ocean: A numerical model for oceanic and coastal waters. *Journal of Geophysical Research: Oceans*, 110(9), 1–12. <https://doi.org/10.1029/2004JC002780>
- Li, J., Scinocca, J., Lazare, M., McFarlane, N., von Salzen, K., & Solheim, L. (2006). Ocean surface albedo and its impact on radiation balance in climate models. *Journal of Climate*, 19(24), 6314–6333. <https://doi.org/10.1175/JCLI3973.1>
- Liou, K.-N. (2002). *An introduction to atmospheric radiation*. Elsevier.
- Lucht, W., Schaaf, C. B., & Strahler, A. H. (2000). An algorithm for the retrieval of albedo from space using semiempirical BRDF models. *IEEE Transactions on Geoscience and Remote Sensing*, 38(2 II), 977–998. <https://doi.org/10.1109/36.841980>

- Ma, L. X., Wang, F. Q., Wang, C. A., Wang, C. C., & Tan, J. Y. (2015). Investigation of the spectral reflectance and bidirectional reflectance distribution function of sea foam layer by the Monte Carlo method. *Applied Optics*, 54(33), 9863–9874. <https://doi.org/10.1364/ao.54.009863>
- Max, J. J., & Chapados, C. (2009). Isotope effects in liquid water by infrared spectroscopy. III. H₂O and D₂O spectra from 6000 to 0 cm⁻¹. *The Journal of Chemical Physics*, 131(18), 184505–184511. <https://doi.org/10.1063/1.3258646>
- Mlawer, E. J., & Clough, S. A. (1998). Shortwave and longwave enhancements in the rapid radiative transfer model 1992. *Proceedings of the Seventh Atmospheric Radiation Measurement (ARM) Science Team Meeting* (pp. 409–413). Retrieved from http://www.arm.gov/publications/proceedings/conf07/extended_abs/mlawer_ej.pdf?i
- Mobley, C. D. (1994). *Light and water: Radiative transfer in natural waters*. Academic Press.
- Monahan, E. C., & O'Muircheartaigh, I. G. (1980). Optimal power-law description of oceanic whitecap coverage dependence on wind speed. *Journal of Physical Oceanography*, 10(12), 2094–2099. [https://doi.org/10.1175/1520-0485\(1980\)010<2094:OPLDOO>2.0.CO;2](https://doi.org/10.1175/1520-0485(1980)010<2094:OPLDOO>2.0.CO;2)
- Monahan, E. C., & O'Muircheartaigh, I. G. (1986). Whitecaps and the passive remote sensing of the ocean surface. *International Journal of Remote Sensing*, 7(5), 627–642. <https://doi.org/10.1080/01431168608954716>
- Moore, K. D., Voss, K. J., & Gordon, H. R. (1998). Spectral reflectance of whitecaps: Instrumentation, calibration, and performance in coastal waters. *Journal of Atmospheric and Oceanic Technology*, 15(2), 496–509. [https://doi.org/10.1175/1520-0426\(1998\)015<0496:SROWIC>2.0.CO;2](https://doi.org/10.1175/1520-0426(1998)015<0496:SROWIC>2.0.CO;2)
- Moore, K. D., Voss, K. J., & Gordon, H. R. (2000). Spectral reflectance of whitecaps: Their contribution to water-leaving radiance. *Journal of Geophysical Research*, 105(C3), 6493–6499. <https://doi.org/10.1029/1999jc900334>
- Morel, A., Antoine, D., & Gentili, B. (2002). Bidirectional reflectance of oceanic waters: Accounting for Raman emission and varying particle scattering phase function. *Applied Optics*, 41(30), 6289–6306. <https://doi.org/10.1364/ao.41.006289>
- Morel, A., & Gentili, B. (1993). Diffuse reflectance of oceanic waters. II. Bidirectional aspects. *Applied Optics*, 32(33), 6864–6879. <https://doi.org/10.1364/AO.32.006864>
- Morel, A., & Gentili, B. (1996). Diffuse reflectance of oceanic waters. III. Implication of bidirectionality for the remote-sensing problem. *Applied Optics*, 35(24), 4850–4862. <https://doi.org/10.1364/AO.35.004850>
- Morel, A., Gentili, B., Claustre, H., Babin, M., Bricaud, A., Ras, J., & Tièche, F. (2007). Optical properties of the “clearest” natural waters. *Limnology & Oceanography*, 52(1), 217–229. <https://doi.org/10.4319/lo.2007.52.1.0217>
- Morel, A., & Maritorena, S. (2001). Bio-optical properties of oceanic waters: A reappraisal. *Journal of Geophysical Research: Oceans*, 106(C4), 7163–7180. <https://doi.org/10.1029/2000jc000319>
- Mukherjee, L., Zhai, P.-W., Hu, Y., & Winker, D. M. (2018). Single scattering properties of non-spherical hydrosols modeled by spheroids. *Optics Express*, 26(2), A124–A135. <https://doi.org/10.1364/oe.26.00a124>
- Nakamura, Y., & Oka, A. (2019). CMIP5 model analysis of future changes in ocean net primary production focusing on differences among individual oceans and models. *Journal of Oceanography*, 75(5), 441–462. <https://doi.org/10.1007/s10872-019-00513-w>
- NASA Goddard Space Flight Center, O. B. P. G. (2014). *Sea-viewing wide field-of-view sensor (SeaWiFS) ocean color data*. NASA Ocean Biology Distributed Active Archive Center (OB.DAAC). https://doi.org/10.5067/ORBVIEW-2/SEAWIFS_OC.2014.0
- Nicolas, J. M., Deschamps, P. Y., & Frouin, R. (2001). Spectral reflectance of oceanic whitecaps in the visible and near infrared: Aircraft measurements over open ocean. *Geophysical Research Letters*, 28(23), 4445–4448. <https://doi.org/10.1029/2001GL013556>
- Ohlmann, J. C., Siegel, D. A., & Mobley, C. D. (2000). Ocean radiant heating. Part I: Optical influences. *Journal of Physical Oceanography*, 30(8), 1833–1848. [https://doi.org/10.1175/1520-0485\(2000\)030<1833:ORHPIO>2.0.CO;2](https://doi.org/10.1175/1520-0485(2000)030<1833:ORHPIO>2.0.CO;2)
- Park, Y. J., & Ruddick, K. (2005). Model of remote-sensing reflectance including bidirectional effects for case 1 and case 2 waters. *Applied Optics*, 44(7), 1236–1249. <https://doi.org/10.1364/AO.44.001236>
- Payne, R. E. (1972). Albedo of the sea surface. *Journal of the Atmospheric Sciences*, 29(5), 959–970. [https://doi.org/10.1175/1520-0469\(1972\)029<0959:aotss>2.0.co;2](https://doi.org/10.1175/1520-0469(1972)029<0959:aotss>2.0.co;2)
- Pope, R. M., & Fry, E. S. (1997). Absorption spectrum (380–700 nm) of pure water. II. Integrating cavity measurements. *Applied Optics*, 36(33), 8710–8723. <https://doi.org/10.1364/AO.36.008710>
- Preisendorfer, R. W., & Mobley, C. D. (1986). Albedos and glitter patterns of a wind-roughened sea surface. *Journal of Physical Oceanography*, 16(7), 1293–1316. [https://doi.org/10.1175/1520-0485\(1986\)016<1293:AAGPOA>2.0.CO;2](https://doi.org/10.1175/1520-0485(1986)016<1293:AAGPOA>2.0.CO;2)
- Ramon, D., Steinmetz, F., Jolivet, D., Compiègne, M., & Frouin, R. (2019). Modeling polarized radiative transfer in the ocean-atmosphere system with the GPU-accelerated SMART-G Monte Carlo code. *Journal of Quantitative Spectroscopy and Radiative Transfer*, 222(223), 89–107. <https://doi.org/10.1016/j.jqsrt.2018.10.017>
- Roesler, C. S., & Perry, M. J. (1995). In situ phytoplankton absorption, fluorescence emission, and particulate backscattering spectra determined from reflectance. *Journal of Geophysical Research*, 100(C7), 279–294. <https://doi.org/10.1029/95jc00455>
- Ross, V., & Dion, D. (2007). Sea surface slope statistics derived from Sun glint radiance measurements and their apparent dependence on sensor elevation. *Journal of Geophysical Research*, 112(9), 1–11. <https://doi.org/10.1029/2007JC004137>
- Roy, S., Sathyendranath, S., Bouman, H., & Platt, T. (2013). The global distribution of phytoplankton size spectrum and size classes from their light-absorption spectra derived from satellite data. *Remote Sensing of Environment*, 139, 185–197. <https://doi.org/10.1016/j.rse.2013.08.004>
- Rutan, D. A., Kato, S., Doelling, D. R., Rose, F. G., Nguyen, L. T., Caldwell, T. E., & Loeb, N. G. (2015). CERES synoptic product: Methodology and validation of surface radiant flux. *Journal of Atmospheric and Oceanic Technology*, 32(6), 1121–1143. <https://doi.org/10.1175/JTECH-D-14-00165.1>
- Rutan, D. A., Rose, F., Roman, M., Manalo-Smith, N., Schaaf, C., & Charlock, T. (2009). Development and assessment of broadband surface albedo from clouds and the Earth's radiant energy system clouds and radiation swath data product. *Journal of Geophysical Research*, 114(8), 1–19. <https://doi.org/10.1029/2008JD010669>
- Rutledge, C. K., & Smith, W. L. (2003). Multi-year observations of shortwave and longwave radiation at the CERES ocean validation site. *International Geoscience and Remote Sensing Symposium (IGARSS)*, 5(C), 3025–3027. <https://doi.org/10.1109/igarss.2003.1294669>
- Sancer, M. I. (1969). Shadow-corrected electromagnetic scattering from a randomly rough surface. *IEEE Transactions on Antennas and Propagation*, 17(5), 577–585. <https://doi.org/10.1109/TAP.1969.1139516>
- Sayer, A. M., Thomas, G. E., & Grainger, R. G. (2010). A sea surface reflectance model for (A)ATSR, and application to aerosol retrievals. *Atmospheric Measurement Techniques*, 3(4), 813–838. <https://doi.org/10.5194/amt-3-813-2010>
- Schaeppman-Strub, G., Schaeppman, M. E., Painter, T. H., Dangel, S., & Martonchik, J. V. (2006). Reflectance quantities in optical remote sensing—definitions and case studies. *Remote Sensing of Environment*, 103(1), 27–42. <https://doi.org/10.1016/j.rse.2006.03.002>
- Schlick, C. (1992). *Divers éléments pour une synthèse d'images réalistes*. Université Bordeaux. Retrieved from <http://www.theses.fr/1992BOR10625>

- 19 of 19